JOURNAL OF AIRCRAFT
Vol. 46, No. 2, March–April 2009

Prediction of UH-60A Structural Loads Using Multibody Analysis and Swashplate Dynamics

A. Abhishek,[*] Anubhav Datta,[†] and Inderjit Chopra[‡]
University of Maryland, College Park, Maryland 20742

DOI: 10.2514/1.35076

The first part of this paper compares three rotor blade structural dynamic formulations: a finite element formulation with modal reduction, a full finite element formulation without modal reduction, and a multibody-based full finite element formulation for arbitrary large deformations. The second part of this paper studies the effect of swashplate dynamics on blade loads and servo-actuator loads. In all cases, measured airloads, damper force, and control pitch angles from the UH-60A flight tests are used to predict and analyze the structural loads. In the first part, the emphasis is on the validation of a multibody formulation, which is first verified with analytical solutions for beams undergoing hypothetical large deformations (elastica), then validated with the Princeton beam large deformation tests, and then finally used to predict the UH-60A structural loads. Two flight conditions are considered: a high-speed, high-vibration flight and a highly loaded dynamic stall flight. Predictions from the multibody analysis are compared with the full finite element and finite element based modal methods. It is observed that the predicted blade loads do not show any significant difference between the three formulations. In the second part, the four-bladed multibody rotor model is coupled to a swashplate-servo model to predict servo loads and to study the effect of swashplate dynamics on blade loads. It is observed that the higher frequencies of servo loads, 8/rev and 12/rev for this rotor, require modeling the swashplate dynamics. The low-frequency component, which is a dominant 4/rev load for this rotor, is less affected by swashplate dynamics and is determined primarily by the accuracy of the 3, 4, and 5/rev pitch-link loads. The 3–5/rev pitch-link loads, and in general the structural loads on the rotor blade, are not affected by swashplate dynamics.

Nomenclature

C_{s_a} = damping of the aft servo
C_{s_f} = damping of the forward servo
C_{s_l} = damping of the lateral servo
E = modulus of elasticity
F_z = force in z direction
I = moment of inertia of the beam
I_{xx} = moment of inertia of the swashplate about x axis
I_{yy} = moment of inertia of the swashplate about y axis
I_{zz} = moment of inertia of the swashplate about z axis
K_{s_a} = stiffness of the aft servo
K_{s_f} = stiffness of the forward servo
K_{s_l} = stiffness of the lateral servo
L = length of the beam
M = bending moment
m = mass of the swashplate
P = load applied
P_i = pitch link load of the ith blade
P_x = moment in x direction, $+ve$ roll left
P_y = moment in y direction, $+ve$ nose up
R_a = aft link load
R_f = forward link load
R_l = lateral link load
s = distance measured along the deflection curve
v_f = deflection for the forward servo
v_l = deflection for the lateral servo
v_a = deflection for the aft servo
w = vertical deflection of a point on the beam
y_f = prescribed deflection for the forward servo
y_l = prescribed deflection for the lateral servo
y_a = prescribed deflection of the aft servo
z = vertical deflection of the swashplate
α_x = longitudinal tilt, $+ve$ pitch up
α_y = lateral tilt, $+ve$ roll left
δ_w = vertical displacement of the beam tip
δ_u = axial foreshortening of the beam tip
θ = angle of rotation of the deflection curve
θ_b = rotation of the end of the beam
κ = curvature of the beam
ρ = radius of curvature of the beam
ϕ = azimuthal location of forward servo measured with respect to 90 deg azimuthal location
ψ = azimuthal location
Ω = rotational speed of the rotor
ω_x = angular velocity of the swashplate about body x axis
ω_y = angular velocity of the swashplate about body y axis
ω_z = angular velocity of the swashplate about body z axis

Introduction

THERE are two objectives for this paper: 1) compare three progressively refined rotor blade structural dynamics formulations for the prediction of structural loads for a given set of aerodynamic forcing, and 2) study the effect of coupled rotor-swashplate dynamics on the prediction of servo loads and rotor blade structural loads.

The first part of this paper compares the following three formulations: 1) a second-order nonlinear beam finite element method (FEM) with modal reduction, 2) a second-order nonlinear beam FEM without modal reduction, and 3) a second-order nonlinear beam FEM within a multibody formulation. These are referred to as FEM with modal, full FEM, and the multibody method. The last formulation offers two advantages. First, the use of local frames compensates for the second-order assumption and allows for arbitrary large deformations. Second, modeling the root end rigid linkages accounts for their exact kinematics. The goal is to study

---

Received 21 November 2007; revision received 3 December 2008; accepted for publication 16 December 2008.

[*] Graduate Research Assistant, Department of Aerospace Engineering.

[†] Rotorcraft Dynamicist, Department of Aerospace Engineering; currently Eloret Corporation, NASA Ames Research Center.

[‡] Department of Aerospace Engineering; currently Alfred Gessow Professor and Director, Alfred Gessow Rotorcraft Center. Fellow AIAA.

whether any improvements are provided by large deformation modeling, and the modeling of exact kinematics of the root end lag damper and pitch link on the blade loads. The second part of this paper describes a swashplate model, and studies the effect of swashplate dynamics on servo loads and blade loads. The multibody model is coupled to the swashplate model in this part of the study. In all cases, measured airloads from the U.S. Army/NASA UH-60A flight-test program [1,2] are used for the validation of the analyses. In particular, two flight conditions are selected: a high-speed level flight (counter 8534: 158 kt, $\mu = 0.368$, $C_W/\sigma = 0.0783$), and a high-altitude dynamic stall flight (counter 9017: 101 kt, $\mu = 0.237$, $C_W/\sigma = 0.135$). The blade root pitch control angles for these flight conditions are relatively large (counter 8534: $\theta_0 = 14.31$, $\theta_{1c} = 4.5$, $\theta_{1s} = -10.5$ deg and counter 9017: $\theta_0 = 12$, $\theta_{1c} = 7$, $\theta_{1s} = -7$ deg).

For an n-bladed rotor, prediction of servo loads in the fixed frame requires accurate prediction of $(np \pm 1)/\text{rev}$ harmonics of the pitch-link loads in the rotating frame, where $p = 1, 2, 3$, and so on. The state of the art in predicted pitch-link loads for the UH-60A helicopter indicate that 3, 4, and 5/rev, and in general the higher harmonics, are not satisfactorily predicted (Fig. 1). The structural dynamics models of current rotor comprehensive analyses predict the flap bending moments correctly for all harmonics (up to 10/rev). The torsion and chord bending moments are comparatively less accurate. The lower harmonics (up to 3/rev) are satisfactory. The higher harmonics (4/rev and above) show significant discrepancies.

Several researchers have calculated the full-scale UH-60A structural loads using airloads measured in flight tests [3–6]. Datta and Chopra [3,4] solved the second-order accurate nonlinear beam equations using a finite element method with modal reduction. Generally, 8–10 modes were sufficient for converged results. Ormiston [5] and Ho et al. [6] used a full FEM with no modal reduction and a multibody formulation to account for large deformations. For the common flight conditions, the imposed airloads, damper force, and rotor properties were identical in [3–6]. The predicted flap bending moments from the different analyses showed similar trends. Predicted chord bending moments, torsion moments, and pitch-link load differed for the higher harmonics (4/rev and above). Predictions from both methods differed from test data for these harmonics. Conceptually, the measured airloads problem (also termed the mechanical airloads problem) allows one to assess the accuracy of the structural model separately from the airloads model. The technique was first applied by Sweers in 1968 for the XH-51A compound helicopter [7]. More recently, it has been applied by Esculier and Bousman [8] on the CH-34 rotor and by Torok and Goodman on the model UH-60A rotor [9]. In practice, the measured airloads problem can pose significant difficulties. The natural frequencies of the blades often lie close to the forcing harmonics and, because the imposed airloads do not change with the calculated response, there is zero aerodynamic damping in the system. Thus, even though uncontaminated with errors associated with predicted airloads, the measured airloads solution can be extremely sensitive to small differences in modeling, input parameters, and unavoidable errors in measured airloads and their interpolation, factors which are either nonexistent or insignificant for fully coupled solutions.

Fully coupled solutions (i.e., structural dynamics, aerodynamics, and trim) are obtained using comprehensive analysis with lifting-line aerodynamic models or, more recently, with comprehensive analysis coupled to computational fluid dynamics (CFD) analyses. The state of the art in predicted structural loads of the UH-60A for a range of level flight conditions using CFD/comprehensive analysis coupling is given in [4]. The principal discrepancies in predicted structural loads from this coupled solution were observed to be consistent with those obtained using measured airloads, that is, the 3/rev and higher harmonics of chord bending, torsion, and pitch-link loads were

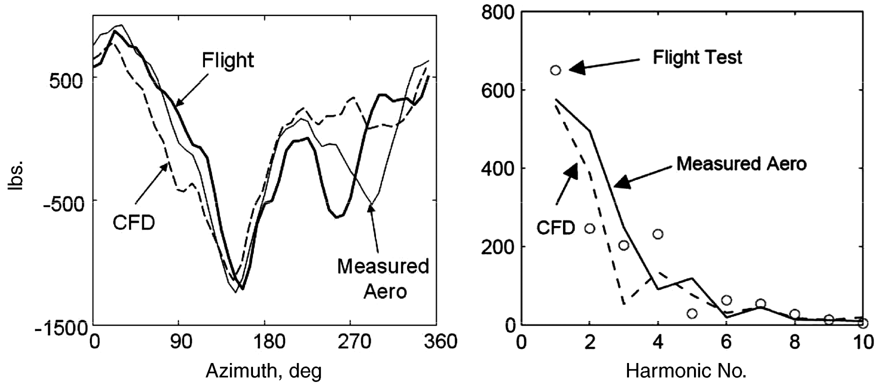

a) High-speed flight

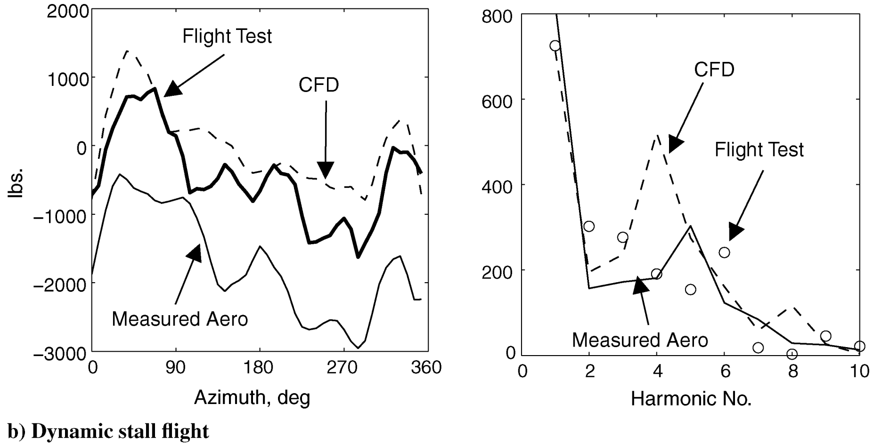

b) Dynamic stall flight

Fig. 1 State of the art in predicted pitch-link loads using measured aerodynamic loads and CFD-coupled (University of Maryland Advanced Rotorcraft Code–University of Maryland Transonic Unsteady Rotor Navier Stokes) analysis for UH-60A: a) high-speed flight (C8534: $C_W/\sigma = 0.0783$, $\mu = 0.368$), b) dynamic stall flight (C9017: $C_W/\sigma = 0.135$, $\mu = 0.237$) [4].

unsatisfactory. The higher harmonic torsion loads in particular are critical for predicting the peak servo loads in the fixed frame. The dominant harmonic in the servo loads is the 4/rev, which is determined by 3, 4, 5/rev pitch-link load.

The focus of the present investigation is on structural dynamics. The goal is to refine the structural model from [3,4] to account for the unmodeled dynamics associated with 1) large deformations, 2) exact lag-damper and pitch-link kinematics and, 3) the effect of swashplate dynamics. The first two refinements are carried out by adopting a multibody dynamics approach. The third refinement is carried out by incorporating a 3-degrees-of-freedom (longitudinal tilt, lateral tilt, and heave motion) swashplate dynamics model. The multibody model is used to consistently compare the three structural dynamics formulations for the same set of model parameters and measured airloads. This is the first objective of the paper. The swashplate model is coupled to the rotor model to study the effect of swashplate dynamics on blade loads and servo loads. This is the second objective of the paper.

Rotor Structural Dynamics Model

Arbitrary large deformations of a flexible beam can be modeled in two ways: 1) using a geometrically exact beam theory [10,11], and 2) using a second-order nonlinear beam theory within a multibody formulation [12,13]. The latter uses additional frames attached locally to a set of individual beam finite elements, within which the elements undergo only moderate (second-order) elastic deformations. The second approach has been followed in this paper.

Multibody Formulation with Full Finite Element Method

The rotor blades and supporting structures are first divided into several bodies, rigid and flexible. Each flexible body is discretized into several finite elements. The rotor is modeled as a second-order nonlinear Euler–Bernoulli beam with axial elongation and elastic twist modeled as quasi coordinates [14–16]. The current formulation incorporates additional frames of reference at the individual beam element level. Arbitrary large deformations of the beam can be accommodated by the finite motion of the frames attached to individual elements while the elastic deformations within each element remain moderate. The rigid body motion of the frames involves large rotations and translations in space. The rotor pitch control angles are imposed as linear displacements at the bottom of the pitch links and are adjusted iteratively to generate the measured root pitch angles. The measured damper force is imposed in a direction based on the exact kinematics of the damper as determined by its configuration and the instantaneous location of blade attachment point.

Equations of motion are developed using Kane's method [17], which are then solved in time using Newmark's method with Hilber–Hughes–Taylor correction [18]. Newmark's method is second-order accurate in time, unconditionally stable, and requires the storage of information for only one time step. Note that the current formulation is not applicable to configurations with arbitrary topologies, unlike the multibody codes such as DYMORE [19] and MBDyn [20]. On the other hand, because there are no algebraic constraint equations with associated Lagrange multipliers, the resulting formulation can be treated using linearized system analysis tools.

The analysis is first validated against analytical and experimental large deformation data. Two static elasticity problems are considered: 1) the problem of a cantilever elastica with tip moment and tip forcing, and 2) the Princeton beam static test problem involving deflection of cantilever beam data.

Elastica with Tip Moment and Tip Force

The shape of the elastic deflection curve of a cantilever beam undergoing large deflection is called elastica. Assuming that the material of the beam remains linearly elastic, the exact governing differential equation is given by

$$\kappa = \frac{\mathrm{d}\theta}{\mathrm{d}s} = -\frac{M}{EI} \tag{1}$$

where κ is the curvature of the beam at a given section, θ is the angle of rotation of the deflection curve, M is the sectional bending moment, E is the modulus of elasticity, and I is the area moment of inertia of the beam section (Fig. 2). For a beam undergoing large deflections, the differential equation governing the curve takes the following form:

$$\frac{\mathrm{d}^2 w/\mathrm{d}x^2}{[1 + (\mathrm{d}w/\mathrm{d}x)^2]^{\frac{3}{2}}} = -\frac{M}{EI} \tag{2}$$

where w is the transverse deflection of a point on the beam. The exact analytical solution of the elastica with tip moment has been described in [21].

A multibody model of a uniform cantilever beam of length L of 20 ft is developed using 20 elements. The bending stiffness EI is taken to be 9000 $\mathrm{lb} \cdot \mathrm{ft}^2$ and a moment of 2500 $\mathrm{ft} \cdot \mathrm{lb}$ is imposed on the beam tip. The resultant radius of curvature $\rho\,(=1/\kappa)$ is then 3.6 ft. Figure 3a verifies the predicted solution with the analytical solution. For a tip force, the analytical solution takes the form of a transcendental equation involving elliptic integrals which can be evaluated using numerical integration. The solutions are tabulated in [21] and are used in Figs. 3b–3d to verify the current calculations. The tip force is applied such that $PL^2/EI = 5.0$. The vertical tip deflection δ_w, the axial foreshortening δ_u, and angle of rotation θ_b are verified in Figs. 3b–3d.

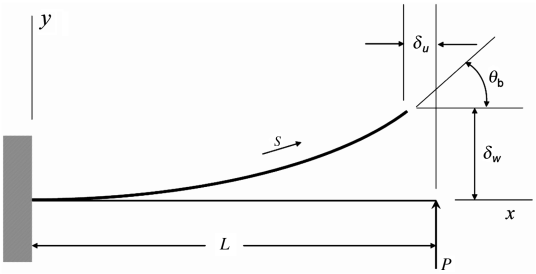

Fig. 2 Large deflections of a cantilever beam due to a tip load.

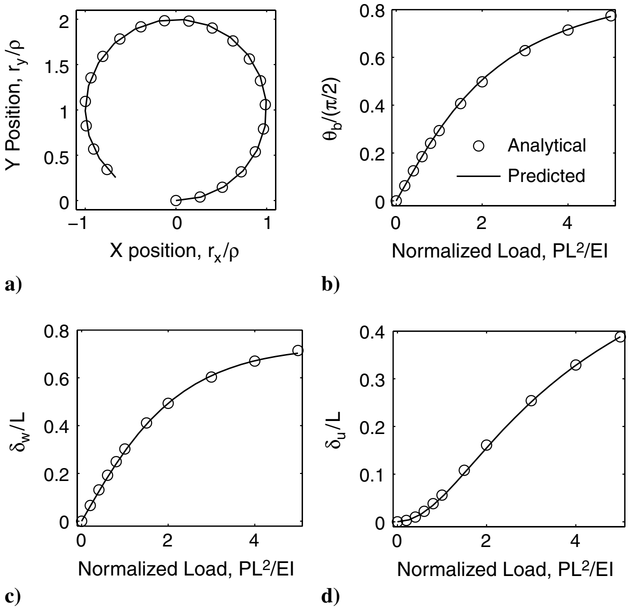

Fig. 3 Elastica a) analytical vs predicted for an aluminum beam of length $L = 20$ ft under tip moment $M = 2500\ \mathrm{ft} \cdot \mathrm{lb}$, $EI = 9000\ \mathrm{lb} \cdot \mathrm{ft}^2$, $\rho = 3.6$ ft; b–d) under tip force—rotation angle θ_b, vertical deflection δ_w, and axial foreshortening δ_u vs normalized tip force.

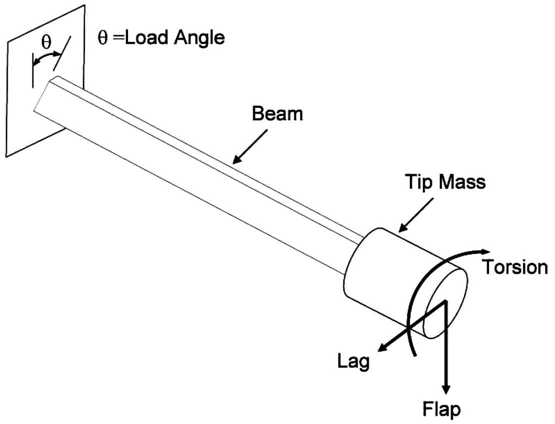

Fig. 4 Schematic representing the Princeton beam test carried out by Dowell and Traybar [23] to study flap-lag-torsion coupling.

Princeton Beam Test

The Princeton beam test, carried out by Dowell et al. [22,23], provides bending and torsional deformation data for an aluminum cantilever beam with rectangular cross section. The beam was rotated to various pitch angles introducing strong flap-lag-torsion coupling (Fig. 4). A multibody model is constructed to simulate the Princeton beam test setup. The geometric and sectional properties used for the simulation were obtained from [22] and are listed in Table 1. Static deformation data from [23] is used to validate the predicted results. Figure 5 compares the predicted flap bending (w/L), lag bending (v/L), and torsion deflections with measured data for a range of tip loading. The deflection in the softer bending direction called flap showed very good correlation with the test data for all loading conditions and for all root pitch angle settings. Predicted torsion deflection is also satisfactory. However, the same is not observed in the stiffer bending direction, and the results are less accurate for the higher loading conditions (3- and 4-lb cases). This is possibly due to the ideal treatment of the support fixture at the root end of the beam. The beam was held using specially fabricated fixtures which were inserted into a milling-machine-type precision indexing chuck, which under higher loading conditions might not provide ideal cantilever conditions [24].

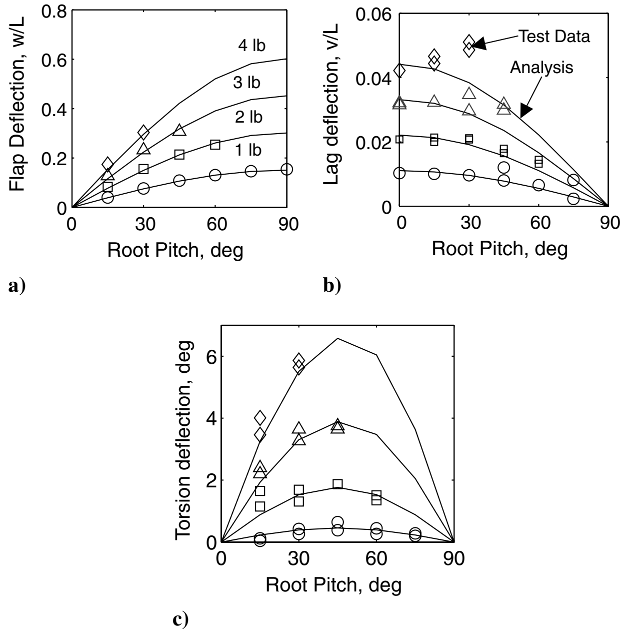

a) b) c)

Fig. 5 Princeton beam test: a) flap bending deflection, b) lag bending deflection, and c) torsion deflection.

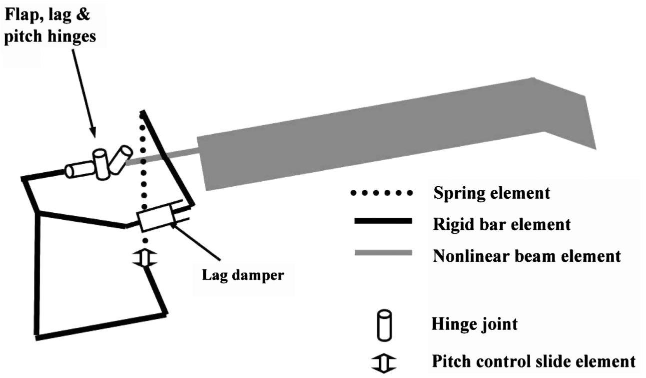

Fig. 6 Schematic of a UH-60A blade structural model.

Classical Formulation with Full Finite Element and Finite Element with Modal Reduction

The classical FEM formulation typically uses a single-body coordinate frame and all deformations and loads are calculated in that particular frame, which are then transformed to an inertial frame. Within a single-body coordinate frame, the second-order almost-exact beam model is accurate up to moderate bending deflections of 15% [12]. The model just described has been used to model the rotor blade as a fully articulated beam with flap and lag hinges coincident at 4.66% span, and is referred to as classical formulation with full FEM. Sweep is incorporated as a center of gravity offset from the straight undeformed elastic axis. The multibody formulation with full FEM can be reduced to classical FEM formulation in several steps. First, the additional frames attached at the element level are removed and all the element-to-element and element-to-body transformation matrices are replaced by identity matrices. All the deformations and forces are now evaluated in a single global reference frame located at the blade hub. Second, the pitch-link spring-damper element undergoing exact kinematics is replaced by an equivalent torsional spring-damper system at the pitch-link attachment point, based on the undeformed geometry. The control angles are now imposed directly. Finally, the lag-damper force is imposed as a set of concentrated forces and moments based on the undeformed geometry of the damper attachment. To reduce the classical full FEM formulation further, an eigenanalysis is performed on the linearized stiffness and mass matrices. The first 10 linearized modes are then chosen to transform the governing equations into the modal coordinate system. This is referred to as FEM with modal reduction.

Table 1 Beam geometric and sectional properties used for the analysis of Princeton beam test

Length, R	20 in.
Width, b	0.5 in.
Height, h	0.125 in.
Density, ρ	0.1014 lb/in.^{3}
Poisson's ratio, ν	0.31
Shear modulus, G	4.0383×10^6 lb/in.^{2}
Young's modulus, E	10.576×10^6 lb/in.^{2}
Polar moment of inertia, J	0.2807 bh^3

UH-60A Rotor Model for Structural Loads

A multibody model of an isolated UH-60A rotor blade is shown in Fig. 6. The measured airloads, damper force, and root pitch angles from the two UH-60A flight-test data points are then used to calculate the structural response. Results obtained using the classical formulations are compared with those obtained using the multibody approach.

The multibody model consists of the flexible blade and rigid root end damper and control linkages. The blade is modeled as a fully articulated beam with flap and lag hinges coincident at 4.66% span using 20 nonlinear beam elements, with each element having an individual frame of reference attached to it. The blade property data are obtained from the NASA (Ames) master database. The swept

Table 2 UH-60A rotor blade operating frequencies, collective angle 14.5 degrees, effective root spring stiffness 1090 ft · lb/ deg

	Frequencies /rev
First chord	0.27
First flap	1.04
Second flap	2.87
First torsion	4.38
Second chord/third flap	4.76
Third flap/second chord	5.22
Fourth flap	7.81
Fifth flap	11.44
Third chord	12.52
Second torsion	12.93

portion of the blade has been modeled using three elements with swept elastic axis. The pitch horn and the hub are modeled using rigid bodies, and the pitch link is modeled as a linear spring-damper element. The pitch-link stiffness is obtained from the measured equivalent root torsion spring stiffness of 1090 ft · lbs/ deg [25], evaluated using the undeformed pitch-horn length. The control angles are imposed via translational displacements at the base of the pitch link, which are then iteratively adjusted to provide the measured root pitch angles. The measured damper force is applied as a follower force. The direction of the damper force is determined by a vector, one end of which is attached to the location where the damper is physically connected to the hub and the other end is attached to the blade at 7.6% of span. The elastomeric bearing stiffness and damping are modeled as linear springs and dampers.

Validation of UH-60 Structural Response and Loads

The multibody formulation is now used to predict the UH-60A structural response and loads at the two flight conditions. The first 10 natural frequencies of the rotor blade at the operating rotational speed are given in Table 2.

High-Speed Flight (8534: $C_W/\sigma = 0.0783$, $\mu = 0.368$)

Figure 7a shows the oscillatory flap angle at the blade root. A damping value of 4% critical in flap is required for good agreement in magnitude and phase. Without this damping, the 1/rev magnitude is overpredicted by 20% (Fig. 7b) and the 1/rev phase shows an error of 40 deg. Note that the effect of damping is primarily on 1/rev rigid motion, the structural loads due to bending remain unaffected. Unavoidable errors in airloads measurements and the issues related to spanwise and chordwise resolution of data can be the source of this discrepancy. More detailed studies on this issues can be found in [3,5]. The root lag angle (Fig. 7c) is affected by the 4% structural damping in flap due to the coupling between flap and lag via the built-in twist angle (9.31 deg) near the root. Figure 7d shows the root pitch angle. It is determined by the flight-test control inputs and the pitch-link flexibility.

The predicted flap bending moments are shown in Fig. 8. The peak-to-peak magnitude of the moments are satisfactorily predicted. The peak moment on the retreating side at the root station (11.3%*R*) is caused by the lag-damper force. The flap moment at the root station is affected by the damper force via the built-in twist angle (9.31 deg) near the root. The moments at all other stations are mostly dependent on the airloads. Figure 9 shows the dominant vibratory harmonics (3–5/rev), both magnitude and phase, varying over span. These harmonics are the primary source of 4/rev vibration in the fuselage. The radial trends are similar, although the magnitudes are overpredicted. The 3/rev is predicted within 5–10% of the flight-test value except at 70%*R*.

The predicted lag bending moments are shown in Fig. 10. The measured damper force waveform is shown in Fig. 10a. The bending moment waveform at the root is almost entirely determined by the damper force. The sharp gradient in the moment waveform at all blade locations near 180–250 deg azimuths is a direct effect of the damper force. Figure 11 shows the harmonics for the lag bending moments (1–5/rev). The magnitude of all the harmonics except 3/rev shows similar trends as test data and generally follows the predictions in [3,5]. The 2 and 4/rev harmonics are underpredicted and the 5/rev is overpredicted. It is important to note that the chord

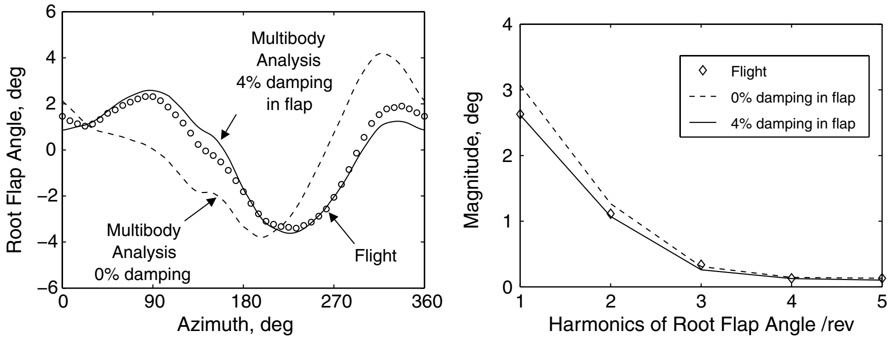

a) Root flap angle, steady removed **b) Magnitude of root flap angle**

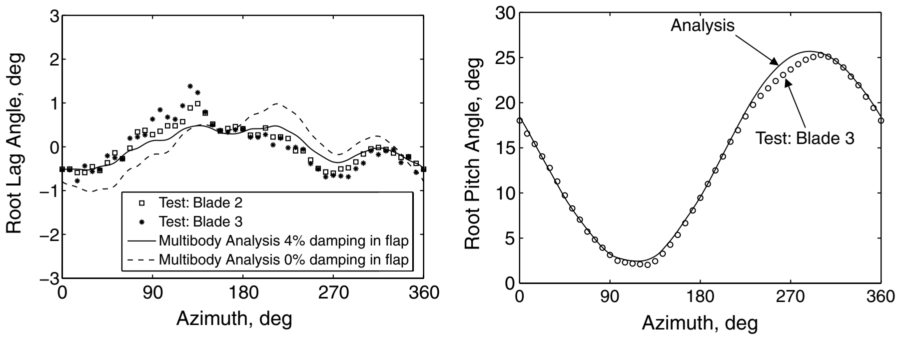

c) Root lag angle, steady removed **d) Root pitch angle**

Fig. 7 Predicted root flap, lag, and torsion angles using measured airloads; effect of damping on the root flap and lag angles; high-speed flight C8534 ($C_W/\sigma = 0.0783$, $\mu = 0.368$).

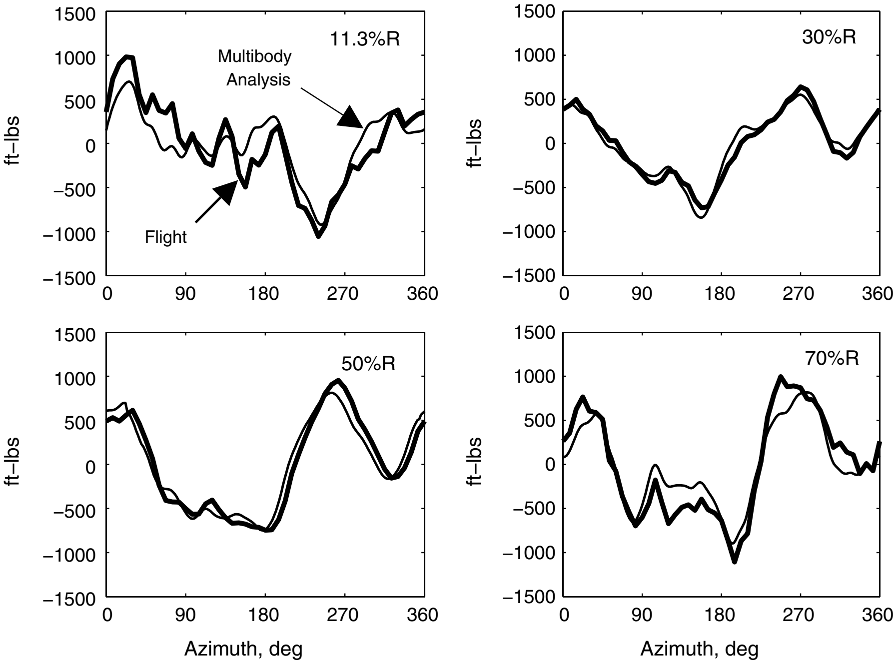

Fig. 8 **Predicted and measured flap bending moments using measured air loads from high-speed flight C8534 ($C_W/\sigma = 0.0783$, $\mu = 0.368$), steady loads removed.**

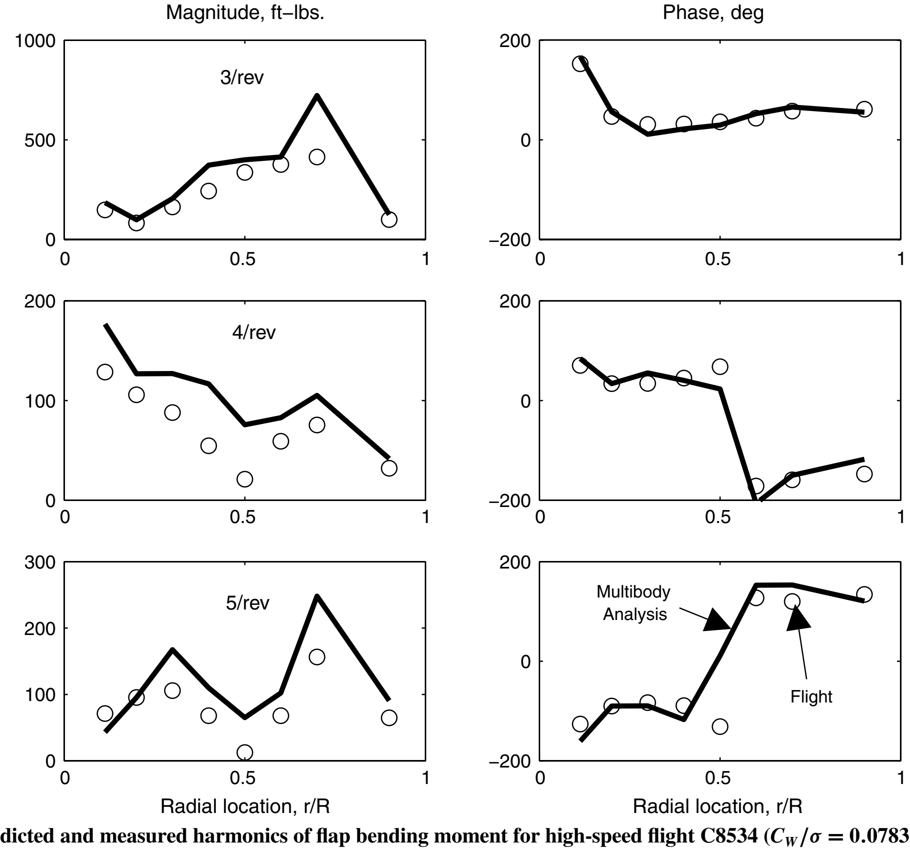

Fig. 9 **Predicted and measured harmonics of flap bending moment for high-speed flight C8534 ($C_W/\sigma = 0.0783$, $\mu = 0.368$).**

force data from the flight test is obtained from the pressure data alone, and hence does not include the effect of viscous drag. However, Datta and Chopra [4] studied the effect of viscous drag from CFD predictions and showed negligible effect in rectifying this discrepancy.

The torsion moment is shown in Fig. 12a. The torsion moment is important for the prediction of the pitch-link load (Fig. 12b), which in turn drives the 4/rev servo loads. Even though the peak-to-peak magnitude is satisfactory, there is significant discrepancy in all harmonics of the waveform, particularly in 3, 4, and 5/rev. The waveform also shows a 15 deg phase discrepancy on the advancing side. Figure 12c shows the harmonic breakup of the pitch-link load, and clearly demonstrates the error in 3, 4, and 5/rev. The pitch-link load is the integrated effect of the spanwise torsion moments, and

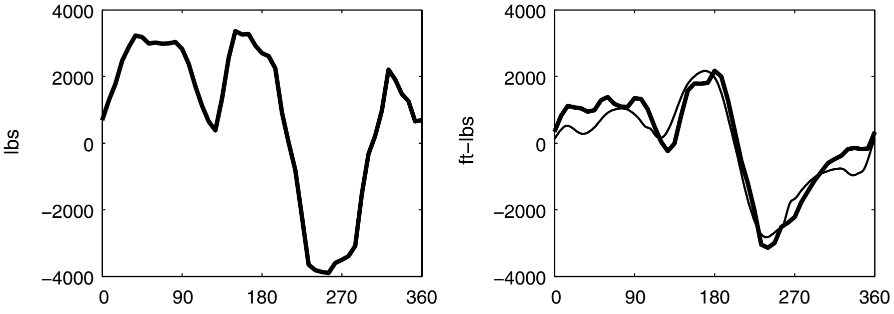

a) Damper force

b) Lag bending at 11.3%R

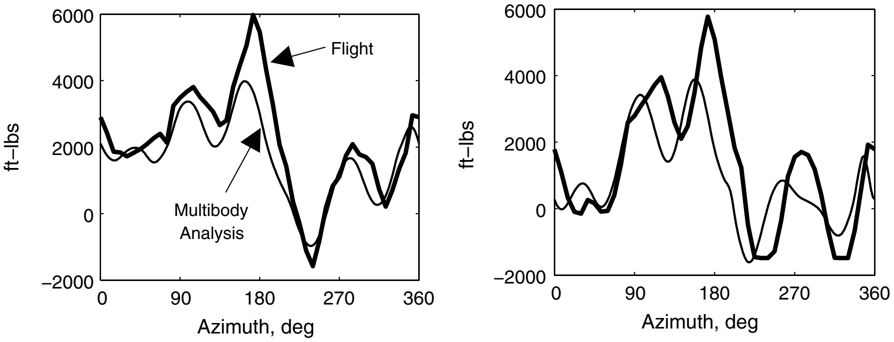

c) Lag bending at 30%R

d) Lag bending at 50%R

Fig. 10 Predicted and measured lag bending moments using measured air loads and damper force from high-speed flight C8534 ($C_W/\sigma = 0.0783$, $\mu = 0.368$), steady loads removed.

hence shows trends similar to the torsion moment. The discrepancy in waveform on the retreating side stems from the errors in higher harmonics (4/rev and higher).

Figure 13 compares the predictions from the multibody, full FEM, and FEM with modal reduction. The comparisons are similar at all radial stations, including near the root, hence predictions at only one radial station are shown. There is no phenomenological difference between any of the predictions. This can be attributed to the fact that the magnitudes of maximum flap and lag deformations at the blade tip are less than 15%R and therefore within the limits of moderate deformation assumptions made in the second-order beam element. The root causes of the discrepancies in higher harmonics of the predictions are clearly unrelated to large deformations or root end kinematics and therefore remain unclear at the present time.

High Altitude Stall Flight (9017: $C_W/\sigma = 0.135$, $\mu = 0.237$)

The oscillatory flap angle at the blade root is shown in Fig. 14a. As in the high-speed case, here a damping value of 5% critical in flap produces good agreement in magnitude and phase (Fig. 14b). Again, note that this additional damping primarily affects the first flap mode and is required only when accurate 1/rev flap deformations are desired. They do not affect the bending moment predictions, which are primarily determined by second and higher modes.

Figure 15 shows the predicted flap bending moments. The phase and the higher harmonic content of the waveforms are satisfactory at all locations. In this flight, the lag bending moment data are available only at the root location (11.3%R). Similar to high-speed flight, it is dominated by the damper force (Figs. 16a and 16b). The torsion moments at 11.3%R and 50%R and the pitch-link load are shown in Figs. 17a–17c, respectively. The 4 and 5/rev harmonics are the source of the torsion oscillations on the retreating blade, which are important for stall prediction at these azimuths [4]. Even though the waveforms appear satisfactory, closer examination of the harmonics (Fig. 17d) reveal a similar 3, 4, and 5/rev discrepancy at high-speed flight. There is a significant 6/rev component in this flight. The analysis fails to predict any of these higher harmonic trends accurately.

A comparison of predictions from the three different formulations again reveal no phenomenological difference. Even with a stall flight, the effect of large deformations in this flight is expected to be even less pronounced. The rotor is trimmed to near zero hub moment in this flight and, as a result, the 1/rev tip flap displacements are close to zero. The higher frequencies of twist are more pronounced in this flight, but their variation is still limited compared to the low-frequency dominated twist in high-speed flight.

Swashplate Dynamics

In this section, a 3-degrees-of-freedom swashplate model is formulated and coupled with the blade model. First, a static load analysis is carried out. The purpose is to estimate the unknown servo stiffnesses. The stiffnesses are estimated by comparing predictions with test data from [25]. Second, a dynamic analysis is carried out using three different swashplate masses: 50, 75, and 85 kg. The actual swashplate mass is unknown, but it is expected to lie in this range, as discussed later in the paper. The measured pitch-link loads are used for this analysis. The purpose is to study the effect of swashplate mass on the servo loads. Note that a zero mass case, with zero damping, reduces to a geometric force transfer problem between the four pitch links and the three servos. Third, a coupled blade-swashplate dynamic analysis is carried out using a simple 7-degrees-of-freedom model. The measured pitch-link loads are no longer used. Instead, the measured airloads are used on the blade, and each blade is now idealized as a single torsion degree-of-freedom system. The spanwise integrated pitching moments are imposed at the blade root as aerodynamic twisting moments. The purpose is to identify the servo steady displacements necessary to obtain the measured blade root pitch angles. Finally, the idealized blade model is replaced with the full finite element based multibody model. This is referred to as the detailed blade-swashplate model.

Swashplate Model

The swashplate is modeled as a thin disk with 3 degrees of freedom: vertical heave, pitch, and roll. It is attached to the four pitch links on the top and three servo actuators at the bottom. The forward stationary link is placed at an azimuthal location of 123°56′, the other two servos are arranged with 90 deg between each of them, as shown in Fig. 18a. The rotating and the nonrotating swashplates are not

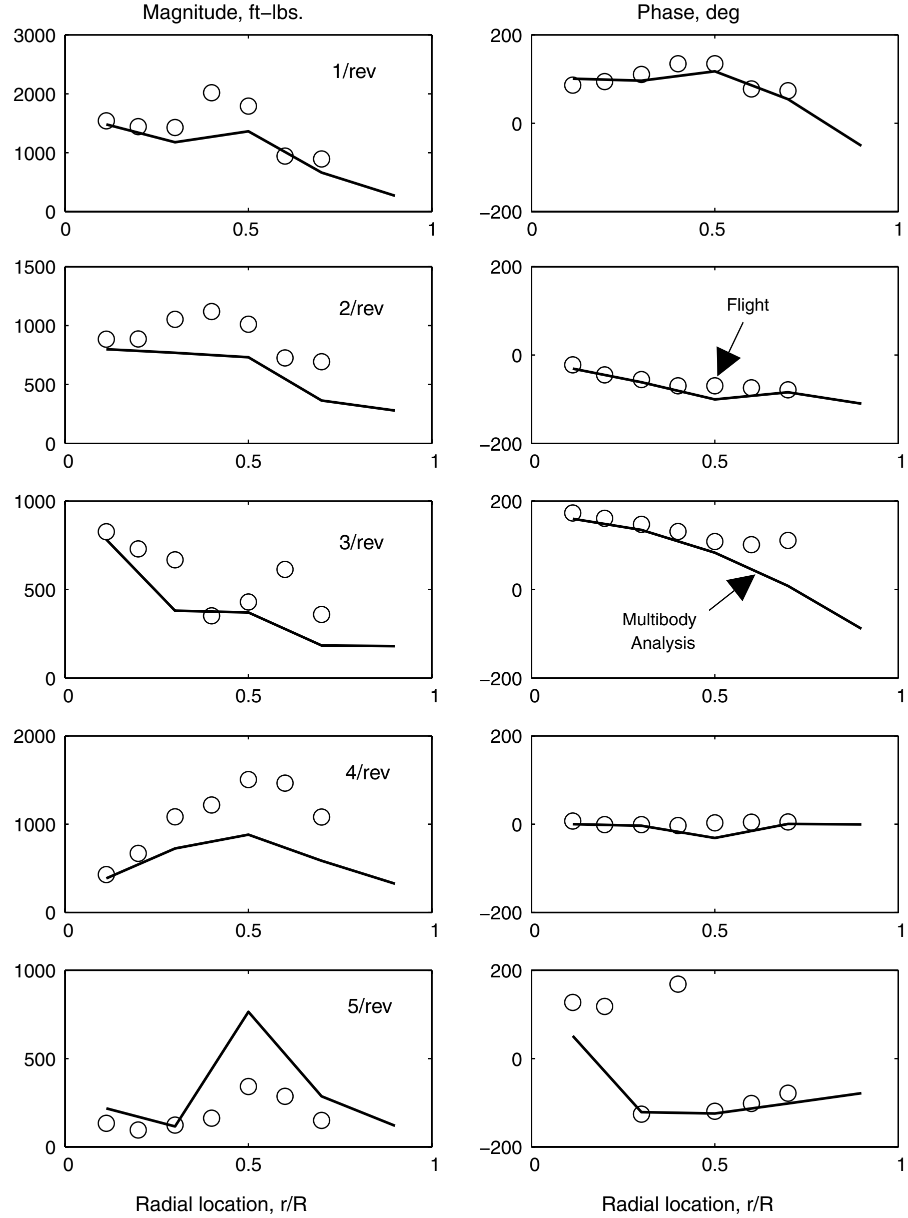

Fig. 11 Predicted and measured harmonics of lag bending moment for high-speed flight C8534 ($C_W/\sigma = 0.0783$, $\mu = 0.368$).

modeled as separate structures, but idealized together as a single functional element. This has three functions: 1) transfer loads between the servos at the bottom and the pitch links on the top, 2) transfer displacements from servos at the bottom to the pitch links on the top, and 3) apply rotating to fixed frame transformation from top to bottom. The four pitch links and the three servos are modeled as linear spring-damper systems.

Consider Fig. 18b. P_1, P_2, P_3, and P_4 are the rotating frame pitch-link loads from blades 1–4. The net force and moments in the fixed frame are then

$$P_x = P_1 r\sin(\psi+\phi) + P_2 r\cos(\psi+\phi) - P_3 r\sin(\psi+\phi) - P_4 r\cos(\psi+\phi) \tag{3}$$

$$P_y = -P_1 r\cos(\psi+\phi) + P_2 r\sin(\psi+\phi) + P_3 r\cos(\psi+\phi) - P_4 r\sin(\psi+\phi) \tag{4}$$

$$P_z = P_1 + P_2 + P_3 + P_4 \tag{5}$$

where r is the radius of the rotating swashplate where the pitch links are attached, P_x, P_y denote the lateral and longitudinal moments, respectively, acting on the swashplate, P_z is the force in the vertical direction, ψ is the blade 1 azimuth angle, and ϕ is the difference in azimuthal location of a blade and its pitch link. The UH-60A rotor has leading-edge pitch links and, when a pitch link is aligned with the forward servo (at azimuth 123°56′), the corresponding blade is at 90 deg azimuth, and thus $\phi = 33°56'$. That is, when a blade is at 0 azimuth, its pitch link is at ϕ.

The three servos must be such that they provide the following net reaction loads on the swashplate:

$$F_z = -m\ddot{z} + P_z \tag{6}$$

$$M_x = -I_{xx}\dot{\omega}_x - (I_{zz} - I_{yy})\omega_y\omega_z + P_x \tag{7}$$

$$M_y = -I_{yy}\dot{\omega}_y - (I_{xx} - I_{zz})\omega_z\omega_x + P_y \tag{8}$$

where ω_x, ω_y, and ω_z are the angular velocities of the swashplate about the x, y, and z axes, respectively, of a reference frame attached to the vehicle (Fig. 18b). These can be related to the swashplate motions as

$$\omega_x = \dot{\alpha}_x - \alpha_y\Omega \tag{9}$$

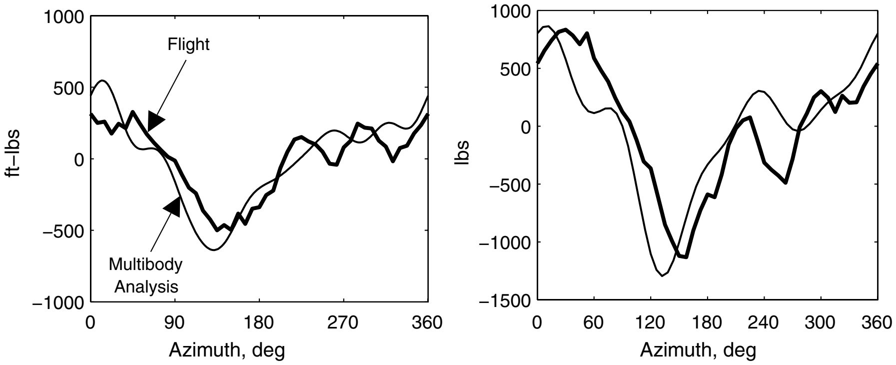

a) Torsional moment at 30%R **b) Pitch-link load**

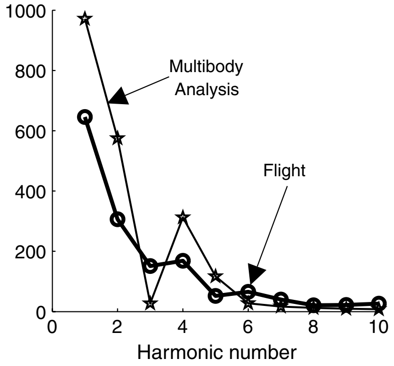

c) Pitch-link load harmonics

Fig. 12 Predicted and measured torsional moment, pitch-link load, and pitch-link load harmonics using measured air loads from high-speed flight C8534 ($C_W/\sigma = 0.0783$, $\mu = 0.368$), steady loads removed.

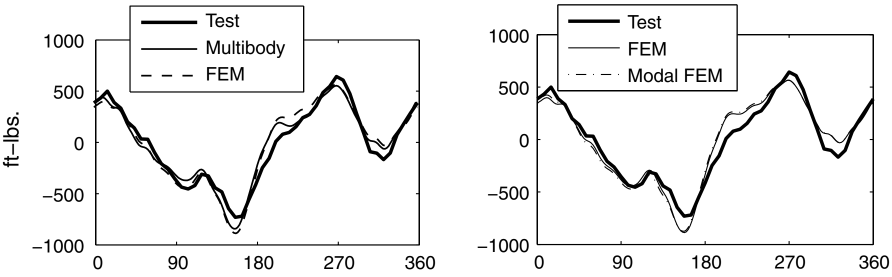

a) Flap bending moment at 30%R

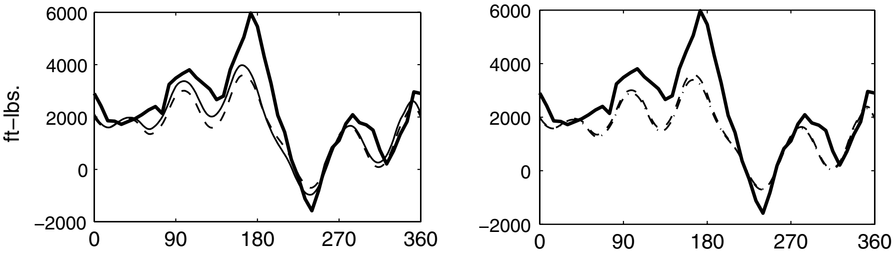

b) Lag bending moment at 30%R

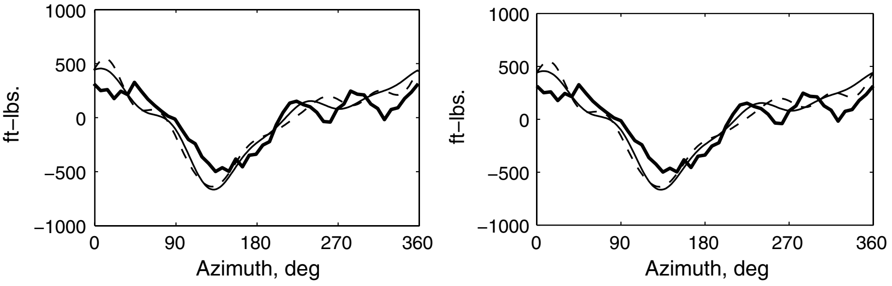

c) Torsion moment at 30%R

Fig. 13 Comparison between multibody, full FEM, and modal FEM predictions for high-speed flight C8534 ($C_W/\sigma = 0.0783$, $\mu = 0.368$).

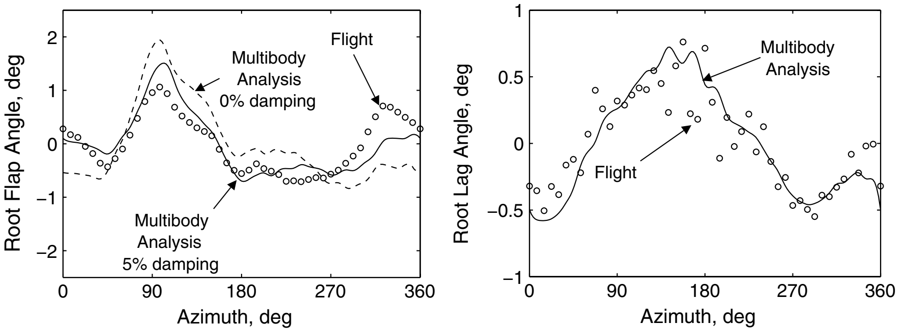

a) Root flap angle, steady removed

b) Root lag angle, steady removed

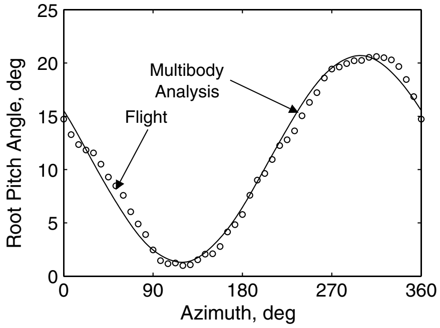

c) Root pitch angle

Fig. 14 Predicted root flap, lag, and torsion angle using measured airloads; effect of damping on the root flap angle; high-altitude stall flight C9017 ($C_W/\sigma = 0.135$, $\mu = 0.237$).

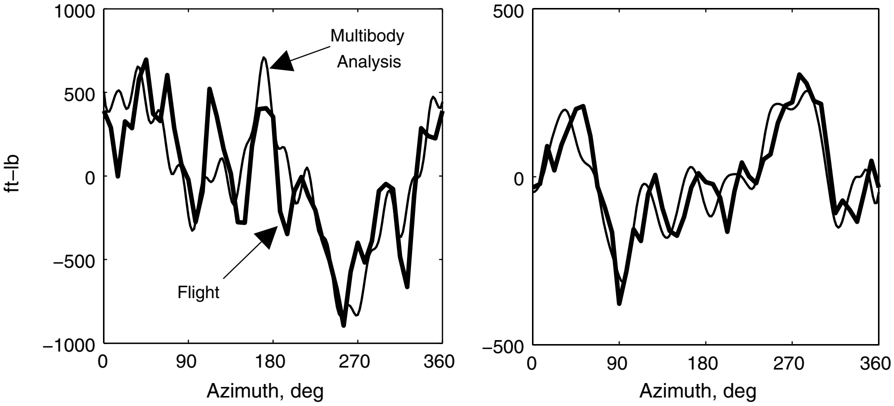

a) 11.3%R

b) 30%R

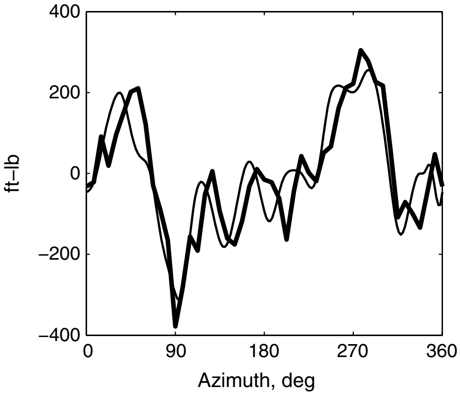

c) 70%R

Fig. 15 Predicted and measured flap bending moment using measured air loads from high-altitude stall flight C9017 ($C_W/\sigma = 0.135$, $\mu = 0.237$), steady loads removed.

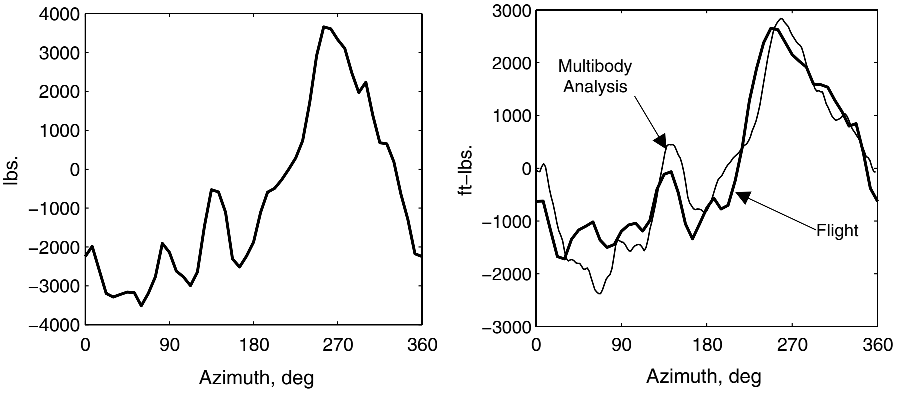

a) Damper force **b) Lag bending moment 11.3%R**

Fig. 16 Predicted and measured lag bending moment using measured air loads from high-altitude stall flight C9017 ($C_W/\sigma = 0.135$, $\mu = 0.237$), steady loads removed.

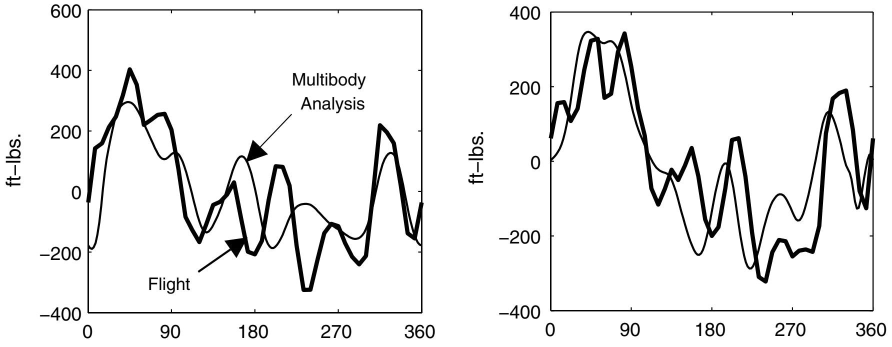

a) Torsional moment at 11.3%R **b) Torsional moment at 50%R**

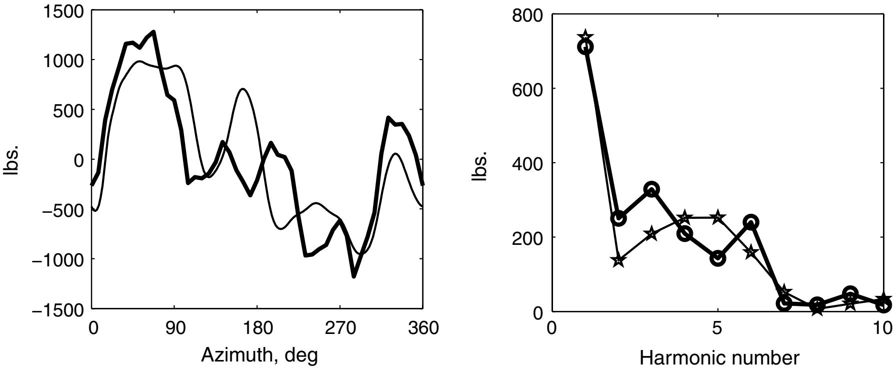

c) Pitch-link load **d) Pitch-link load harmonics**

Fig. 17 Predicted and measured torsional moment, pitch-link load, and pitch-link load harmonics using measured air loads from high-altitude stall flight C9017 ($C_W/\sigma = 0.135$, $\mu = 0.237$), steady loads removed.

$$\omega_x = \dot{\alpha}_y + \alpha_x \Omega \tag{10}$$

$$\omega_z = \alpha_y \dot{\alpha}_x - \alpha_x \dot{\alpha}_y + \Omega \approx \Omega \tag{11}$$

Substituting Eqs. (9–11) in Eqs. (6–8) and using $I_{zz} = I_{xx} + I_{yy}$, results in

$$F_z = -m\ddot{z} + P_z \tag{12}$$

$$M_x = -I_{xx}\ddot{\alpha}_x - I_{xx}\Omega^2\alpha_x + P_x \tag{13}$$

$$M_y = -I_{yy}\ddot{\alpha}_y - I_{yy}\Omega^2\alpha_y + P_y \tag{14}$$

where I_{xx}, I_{yy}, I_{zz}, and m are, respectively, the moments of inertia about x (lateral), y (longitudinal), and z (normal) axes, and the mass of the swashplate. The servo loads causing the preceding net reaction loads are given by

$$R_f = \frac{F_z}{2} + \frac{M_x + M_y}{2r_s}\sin\phi + \frac{M_x - M_y}{2r_s}\cos\phi \tag{15}$$

$$R_l = \frac{M_y\cos\phi - M_x\sin\phi}{r_s} \tag{16}$$

$$R_a = \frac{F_z}{2} + \frac{M_x - M_y}{2r_s}\sin\phi - \frac{M_x + M_y}{2r_s}\cos\phi \tag{17}$$

where r_s is the radius of the stationary part of the swashplate where the servos are attached, and R_f, R_l, and R_a are the servo loads for forward, lateral, and aft servos, respectively. It should be noted that the lateral servo load R_l is independent of F_z because of the asymmetric positioning of the three servos across the swashplate. The forward and aft servos are arranged at diametrically opposite azimuths at approximately 123°56′ and 303°56′, whereas the lateral

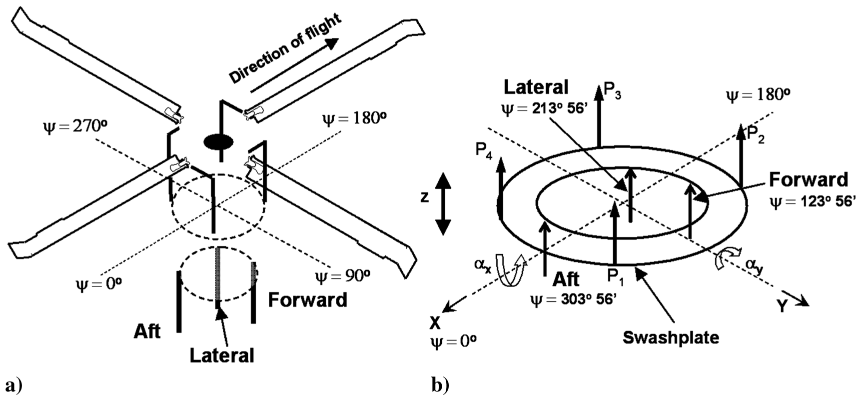

Fig. 18 UH-60A blade–swashplate model a) schematic, b) detailed model with three servo actuators (forward, aft, and lateral) and four pitch links (P_1, P_2, P_3, and P_4); both the rotating and stationary swashplates are of the same size but have been shown to have different sizes for clarity.

servo is halfway at 213°56′ azimuth. Note that, when all the pitch-link loads are the same, that is, $P_1 = P_2 = P_3 = P_4$, then $M_x = M_y = 0$ and $R_l = 0$. The servo deflections needed to produce the desired swashplate motions z, α_x, and α_y are

$$v_f = z + \alpha_x r_s \cos\phi + \alpha_y r_s \sin\phi \tag{18}$$

$$v_l = z - \alpha_x r_s \sin\phi + \alpha_y r_s \cos\phi \tag{19}$$

$$v_a = z - \alpha_x r_s \cos\phi - \alpha_y r_s \sin\phi \tag{20}$$

where v_f, v_l, and v_a denote the forward, lateral, and aft servo deflections. Modeling the servos as linear spring-damper systems, we have

$$R_f = K_{s_f}(v_f - y_f) + C_{s_f}(\dot{v}_f - \dot{y}_f) \tag{21}$$

$$R_l = K_{s_l}(v_l - y_l) + C_{s_l}(\dot{v}_l - \dot{y}_l) \tag{22}$$

$$R_a = K_{s_a}(v_a - y_a) + C_{s_a}(\dot{v}_a - \dot{y}_a) \tag{23}$$

where y_f, y_l, and y_a are a prescribed set of static servo deflections necessary to tilt the swashplate to generate the desired control angles at the blade root.

To obtain the final set of governing equations for the swashplate dynamics, we substitute Eqs. (3–5) in Eqs. (12–14), and then use them in Eqs. (15–17). The resulting expressions are then equated with Eqs. (21–23). The final form of the swashplate equations are expressed as follows:

$$\begin{bmatrix} m & A_1 I_{xx} & B_1 I_{yy} \\ 0 & A_2 I_{xx} & B_2 I_{yy} \\ m & A_3 I_{xx} & B_3 I_{yy} \end{bmatrix} \begin{pmatrix} \ddot{z} \\ \ddot{\alpha}_x \\ \ddot{\alpha}_y \end{pmatrix} + \begin{bmatrix} 2C_{s_f} & 2C_{s_f} r_s \cos(\phi) & 2C_{s_f} r_s \sin(\phi) \\ C_{s_l} & -C_{s_l} r_s \sin(\phi) & C_{s_l} r_s \cos(\phi) \\ 2C_{s_a} & -2C_{s_a} r_s \cos(\phi) & -2C_{s_a} r_s \sin(\phi) \end{bmatrix} \begin{pmatrix} \dot{z} \\ \dot{\alpha}_x \\ \dot{\alpha}_y \end{pmatrix}$$
$$+ \begin{bmatrix} 2K_{s_f} & 2K_{s_f} r_s \cos(\phi) + A_1 I_{xx}\Omega^2 & 2K_{s_f} r_s \sin(\phi) + B_1 I_{yy}\Omega^2 \\ K_{s_l} & -K_{s_l} r_s \sin(\phi) + A_2 I_{xx}\Omega^2 & K_{s_l} r_s \cos(\phi) + B_2 I_{yy}\Omega^2 \\ 2K_{s_a} & -2K_{s_a} r_s \cos(\phi) + A_3 I_{xx}\Omega^2 & -2K_{s_a} r_s \sin(\phi) + B_3 I_{yy}\Omega^2 \end{bmatrix}$$
$$\times \begin{pmatrix} z \\ \alpha_x \\ \alpha_y \end{pmatrix} = \begin{pmatrix} A_1 P_x + B_1 P_y + F_z + 2(K_{s_f} y_f + C_{s_f} \dot{y}_f) \\ A_2 P_x + B_2 P_y + K_{s_l} y_l + C_{s_l} \dot{y}_l \\ A_3 P_x + B_3 P_y + F_z + 2(K_{s_a} y_a + C_{s_a} \dot{y}_a) \end{pmatrix} \tag{24}$$

where,

$$A_1 = \frac{\sin\phi + \cos\phi}{r_s} \qquad A_2 = -\frac{\sin\phi}{r_s} \qquad A_3 = \frac{\sin\phi - \cos\phi}{r_s} \tag{25}$$

$$B_1 = \frac{\sin\phi - \cos\phi}{r_s} \qquad B_2 = \frac{\cos\phi}{r_s} \qquad B_3 = -\frac{\sin\phi + \cos\phi}{r_s} \tag{26}$$

The position of the servos and the pitch links are obtained from [25]. The servo stiffnesses are unknown. They are now identified using the static part of Eq. (24) in the following manner.

Static Loading

The servo stiffnesses are identified by comparing detailed control system stiffness measurements given in [25] with predictions from the preceding formulation. An approximate stiffness value, from [26], is also quoted. Three types of static loading were applied in [25]: 1) collective, 2) reactionless, and 3) cyclic. The same loading conditions are simulated using the preceding analytical model. In the case of collective loading, identical leading-edge-down root pitching moments are imposed in the same direction on all four blades at each azimuth station (+1824 ft · lbs). The moments are transmitted to the swashplate via the pitch links and then to the servos. In the case of reactionless loading, identical root pitching moments are imposed in opposite directions on alternate blades (+1824, −1824, +1824, and −1824 ft · lbs). In the case of cyclic loading, the root pitching moments are imposed in a cyclical manner.

Figure 19a shows that the maximum collective stiffness (imposed moment divided by root twist) occurs near 180 deg but is not symmetric. The model predicts the same behavior. This is caused by the placement of the servos. The stiffness is high in the regions immediately above the servos, and low farther away. The magnitude of prediction depends on the forward and aft servo stiffnesses. The stiffness values of 1.5×10^7 and 0.58×10^7 N/m for forward and aft servos, respectively, provide a good magnitude agreement with test data.

In the case of reactionless loading, the net force and moments on the servos are zero (Fig. 19b). Thus, this configuration isolates the pitch-link stiffness, as none of the servos are deflected. The test data show a higher frequency variation (higher than 1/rev) which is not expected to be predicted by the analysis. This appears to stem from swashplate elastic deformations, which were not included in the model.

In [25], cyclic loading is applied in two steps. In the first step, all blades start with equal loading (1063 ft · lbs), and then the loading on only one set of opposite blades is changed, for example, for blades at 0 and 180 deg. Loading on one blade is increased to 1824 ft · lbs, whereas the loading on the opposite blade is decreased to 303 lbs.

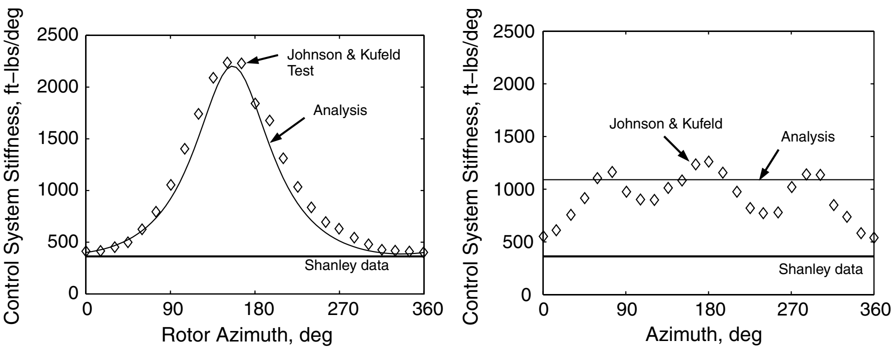

a) Collective **b) Reactionless**

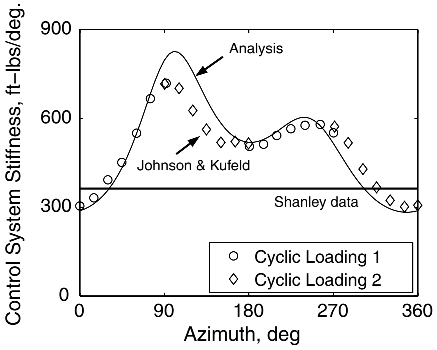

c) Cyclic

Fig. 19 Predicted individual blade stiffness as a function of rotor azimuth for a) collective, b) reactionless, and c) cyclic loading compared with Kufeld and Johnson [25] and Shanley data [26].

The loading on the blades at 90 and 270 deg remain constant. The net loading on the blades are then 1824, 1063, 303, and 1063 ft · lbs. This loading condition is called cyclic loading 1. In the second step, the load change is performed on the other two blades at 90 and 270 deg. The loads on blades at 0 and 180 deg now remain constant. The experimental stiffness values differ marginally; the predictions, of course, are identical. Note that the predictions do not depend on the exact magnitudes of the loading but depend on their variation, however, the test data does because of the nonlinearities associated with loading hysteresis. The lateral servo stiffness is determined as 0.45×10^7 N/m to provide a good magnitude agreement with the cyclic loading data (Fig. 19c).

Dynamic Loading

The mass of the swashplate is not known, hence the Tischenko equation for swashplate mass is used to get an estimate. Tischenko [27] considers that the weight of the swashplate is proportional to the moment of forces coming from the rotor blades. The forces coming from the rotor blades are in turn proportional to $N_b C_b^2 R$. Thus, the mass of the swashplate is given by

$$m = W_{\text{sp}} N_b C_b^2 R \tag{27}$$

where N_b is the number of blades, C_b is the average blade chord, and R is the blade radius. The coefficient of mass for the swashplate W_{sp} is approximately equal to 8 kg/m^3 for most modern helicopters in the UH-60A weight category. Using the UH-60A blade data in the preceding expression, the mass of the swashplate is estimated to be around 75 kg (73 kg, 160.94 lbs).

The measured pitch-link load from blade 2 is now phase shifted for four blades and imposed on the swashplate. The swashplate mass is varied about the estimated value to study its effect on the servo-loads prediction. Figures 20a and 20b compare the predicted servo loads for the two flight conditions with the test data without swashplate dynamics, that is, with swashplate mass set to 0 kg. The servo loads in the high-altitude stall flight are 2–3 times greater than those occurring in the high-speed flight. Therefore, the loads in the high-altitude stall flight are studied further in Fig. 20c. Here, the harmonics of the three servo loads are shown, and they are compared with predictions corresponding to swashplate masses of 0, 50, 75, and 85 kg. Note that, unlike the test data, only integer harmonics of the blade number are expected from the analysis, as the imposed pitch-link loads are kept the same for all blades (only phase shifted) and therefore no blade-to-blade dissimilarity is modeled. It appears that the dynamics of the swashplate can have a significant effect on the servo loads. The frequencies (at 0 deg azimuth) of a 50 kg swashplate are 11.6, 22.4, and 33.4/rev. The frequencies corresponding to 75 and 85 kg masses are 9.48, 18.3, and 27.24/rev, and 8.9, 17.2, and 25.6/rev. Figure 20c shows that the 4/rev servo loads increase in general with an increase in swashplate mass; this is simply because the swashplate motions, which are primarily 4/rev, increase with swashplate inertia as the first natural frequency decreases. The 8 and 12/rev servo loads are more significantly affected by swashplate dynamics. As expected from the frequencies, 8/rev is most sensitive for a 50 kg mass and 12/rev for 85 kg.

The servo loads are predominantly 4/rev and, as noted earlier, the stall flight shows a significantly higher 4/rev content than the high-speed flight. The 4/rev pitch-link load, on the other hand, is higher in high-speed flight than in the stall flight, as shown in Fig. 21. The 4/rev servo loads are the result of 3, 4, and 5/rev pitch-link forcing. The 3/rev forcing is similar in both flight conditions. Thus, it appears that the 4/rev servo loads are dominated by 5/rev pitch-link forcing. The 5/rev pitch-link forcing is significantly higher in the stalled flight than in high speed, and is consistent with the servo loads. The analysis appears to show this trend of the test data. The magnitude of the servo loads are satisfactorily predicted in both flights. Thus, even though the 4/rev forcing on the swashplate is twice as high in high speed, the servo loads are still only half of those in stall flight. This is possibly because the servo loads for this rotor are dominated by 5/rev forcing.

Seven-Degree-of-Freedom Blade–Swashplate Coupled Model

This simple blade–swashplate coupled model is used only to estimate the unknown servo displacements for the two flights that

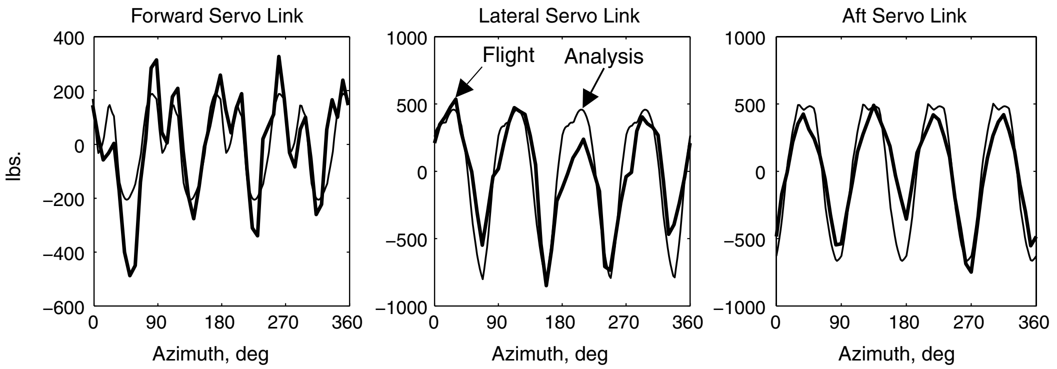

a) Flight 8534

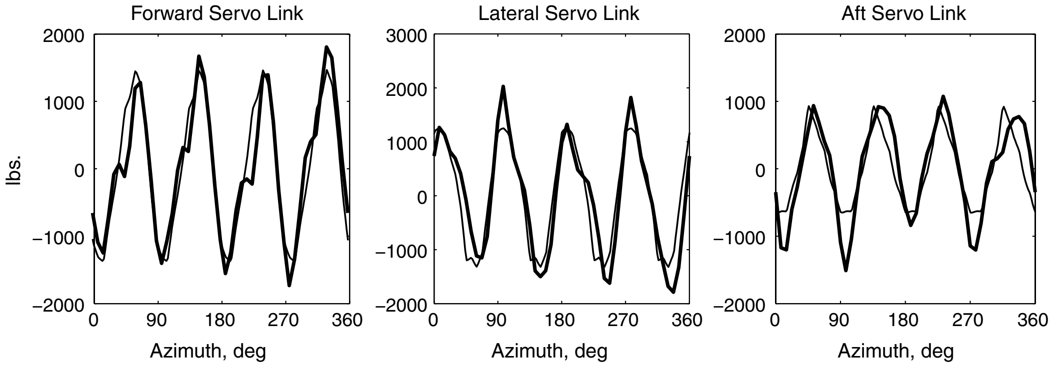

b) Flight 9017

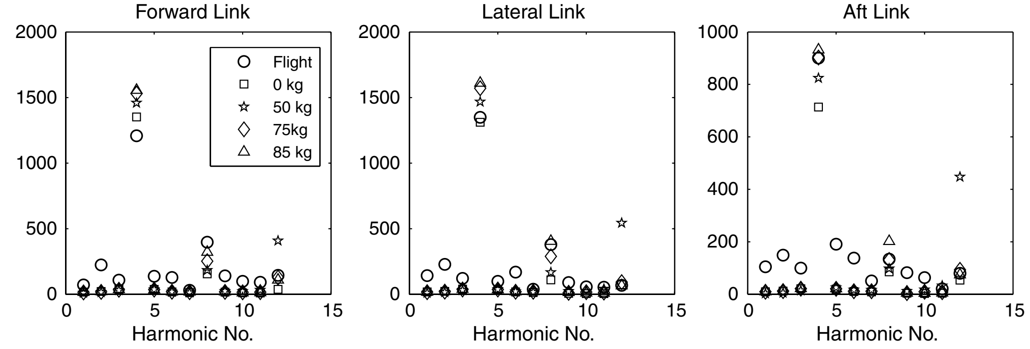

c) Servo link load harmonics for flight 9017

Fig. 20 Predicted swashplate–servo loads using measured pitch-link load, with 0 kg swashplate mass for a) high-speed flight 8534 and b) dynamic stall flight 9017, and c) servo load harmonics for 9017 with swashplate mass of 0, 50, 75, and 85 kg swashplate mass.

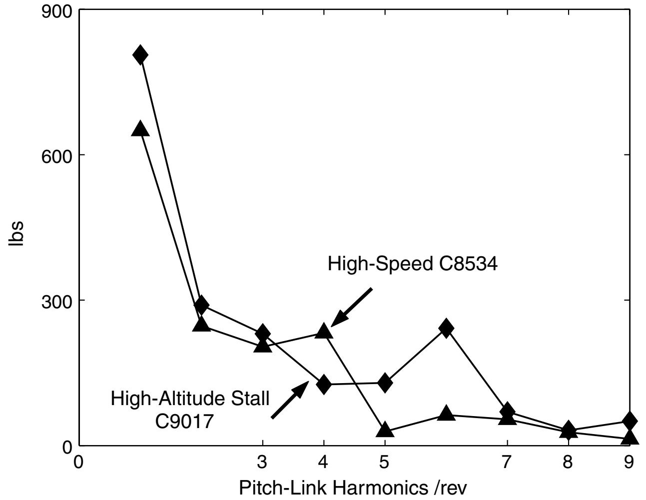

Fig. 21 Flight test results: pitch-link load harmonics compared for high-speed UH-60A flight 8534 ($C_W/\sigma = 0.0783$, $\mu = 0.368$) and high-altitude dynamic stall flight 9017 ($C_W/\sigma = 0.135$, $\mu = 0.237$).

will be studied with the detailed blade model in the next section. Here, each one of the four blades is idealized as a single degree-of-freedom system having only rigid torsion degree of freedom. The first torsion frequency of the UH-60A blades is 4.38/rev, corresponding to a pitch-link stiffness of 2.745×10^6 N/m or, equivalently, a root spring stiffness of 1090 ft · lbs/ deg. The blades are assumed identical. The measured airloads are imposed on the rigid blades as integrated root aerodynamic pitching moment at the pitch bearing.

The steady servo displacements that are required to generate the measured control angles at the bearing can now be calculated. For the high-speed flight, they are 0.3, 0.07, and 0.3%R (1, 0.23, 1 in.) for the forward, lateral, and aft servos, respectively. Figure 22a shows that the preceding values produce a good agreement with the measured blade root pitch angle. Similarly, for the stalled flight, servo displacements of 0.3, 0.045, and 0.25%R (1, 0.14, 0.8 in.) produce the flight-test measured angles. This is shown in Fig. 22b.

In the next section, the detailed blade model is coupled to the swashplate model. The input servo deflections for control angles are those obtained using the simple model in this section.

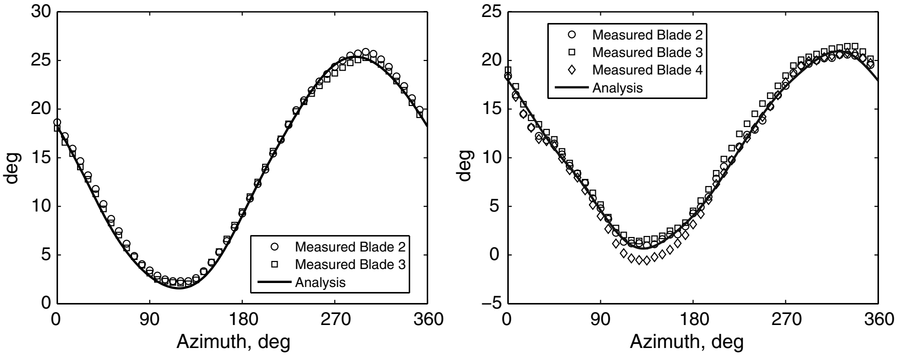

a) Flight 8534 b) Flight 9017

Fig. 22 Predicted blade root pitch angle using steady servo inputs for flight 8534 and 9017, using airloads measured in flight; simple 7-degrees-of-freedom, coupled blade-swashplate dynamic model.

Detailed Finite Element Blade–Swashplate Coupled Model

The swashplate model is coupled to the multibody blade model in this section. The pitch-link load obtained at every time step using the blade model is imposed on the swashplate model and the swashplate motions are calculated. The steady servo deflections below the swashplate are held fixed at values calculated in the previous section. The total swashplate motions are then used for the next time step for the calculation of the blade response. Note that the total motion includes the steady tilt that is necessary to generate the pitch control angles. The blade–swashplate coupled analysis is then carried out until periodicity. The inclusion of the swashplate model in the analysis facilitates the study of effect of cyclic variation of control system stiffness and the swashplate mass on the rotor dynamics. It is observed that the swashplate dynamics have an insignificant effect on the overall dynamics of the rotor (Fig. 23). This is attributed to the fact that the swashplate motions do not have any significant effect on the blade root pitch angle which governs the blade dynamics (Fig. 24).

Figure 25a shows the predicted servo loads for flight 9017 for a swashplate mass of 75 kg. The peak-to-peak forward link load is underpredicted by 40% stemming from a 4/rev error. Figure 25b shows the harmonic breakup of the servo loads. Because the 4/rev and 5/rev pitch-link loads are overpredicted for flight 9017 (Fig. 17d), the underprediction of the forward servo load stems from an underprediction of the 3/rev pitch-link load. The peak-to-peak lateral link load is well predicted, but it shows a 10–20 deg error in the 4/rev phase. The aft servo load is predicted well in both magnitude and phase. It can be observed from Figs. 23 and 25 that swashplate dynamics do not have any effect on the blade loads for this rotor, but affect the servo loads prediction significantly. Figure 25b shows that a deviation of 25% can occur in the magnitude of the 4/rev servo loads and an overprediction of 100–200% in the magnitude of the 4, 8, and 12/rev servo loads depending on the dynamics of the swashplate.

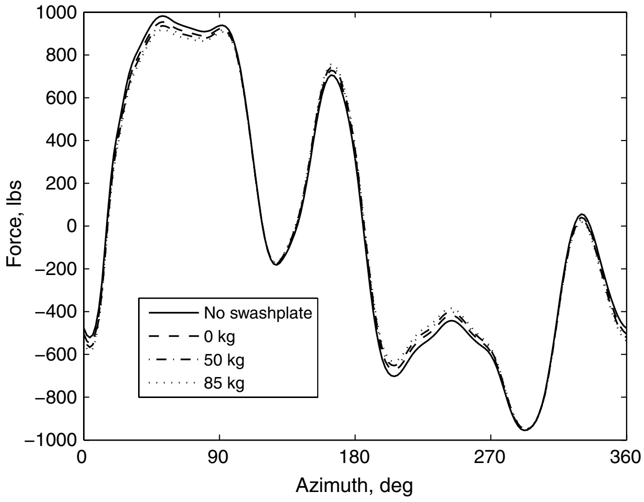

Fig. 23 Effect of swashplate dynamics on the pitch-link load variation for coupled blade–swashplate model for flight 9017.

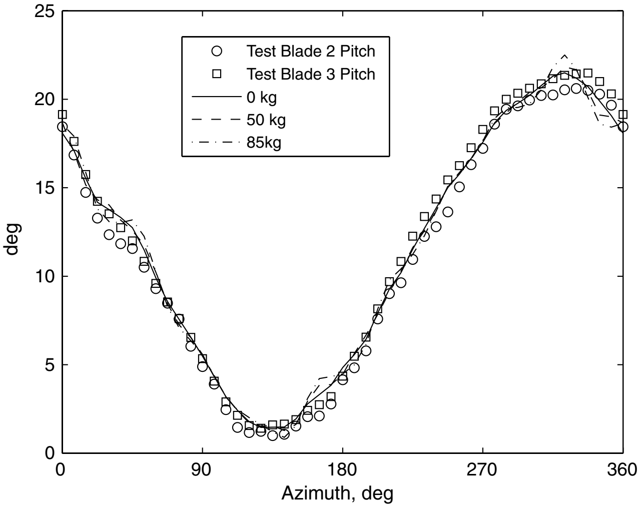

Fig. 24 Effect of swashplate dynamics on the blade root pitch angle for coupled blade–swashplate system for flight 9017.

Conclusions

A detailed finite element multibody structural dynamic analysis has been developed for a rotor-swashplate system. The model is first verified with analytical solutions for large deformation problems. Next, it is validated with static Princeton beam large deformation data. Finally, the full-scale measured airloads from the full-scale UH-60A flight tests are used to calculate the structural loads under two flight conditions: a high-speed high-vibration flight and a high-altitude dynamic stall flight. Selected predictions were systematically compared between three formulations: full finite element with multibody dynamics, full finite element, and finite element with modal reduction. A swashplate model was coupled to the rotor model to study the effect of swashplate dynamics on structural loads. Based on this study, the following key conclusions are drawn.

1) All three of the structural dynamic formulations, multibody, full finite element, and finite element with modal reduction, showed identical prediction of structural loads for the UH-60A rotor at the two flight conditions: a high-speed high-vibration flight (counter 8534: 158 kt, $\mu = 0.368$, $C_W/\sigma = 0.0783$), and a high-altitude dynamic stall flight (counter 9017: 101 kt, $\mu = 0.237$, $C_W/\sigma = 0.135$). The flap bending moment is satisfactory across all harmonics. The chord bending moment is underpredicted in 4/rev and overpredicted in 5/rev. Torsion moment prediction is least

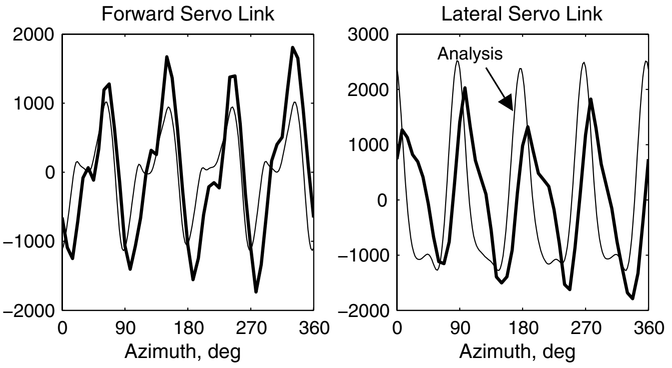

a) Servo loads using swashplate mass of 75kg

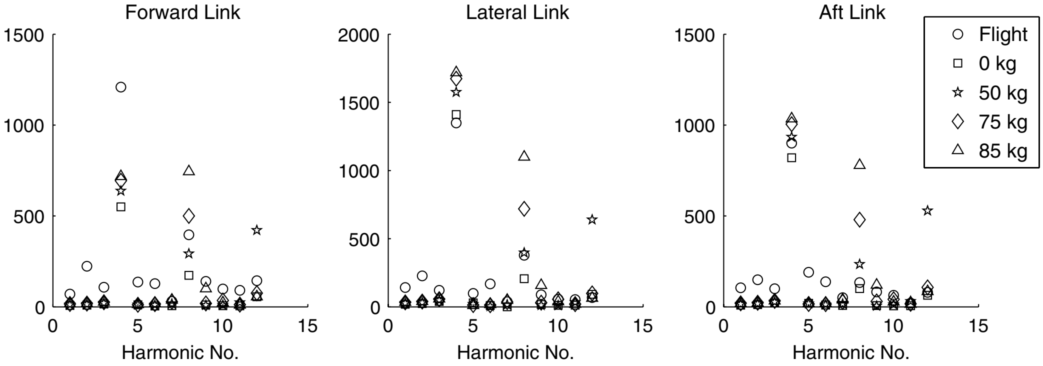

b) Servo loads harmonics

Fig. 25 Predicted and measured servo loads for coupled blade–swashplate system for flight 9017 ($C_W/\sigma = 0.135$, $\mu = 0.237$): a) waveform, using a swashplate mass of 75 kg, and b) harmonics using swashplate masses of 0, 50, and 85 kg.

satisfactory for harmonics 3/rev and higher. The peak-to-peak magnitudes are, however, correct for all loads.

2) The dynamics of the swashplate do not appear to have a significant effect on the prediction of torsion loads on the blade and pitch link. The blade loads, predicted with or without coupled swashplate dynamics, show the same peak-to-peak and higher harmonic content. The cyclic variation of control system stiffness (substantial due to the presence of the servos underneath) does not affect the predicted torsion loads either.

3) The magnitude of servo loads is affected not only by the pitch-link load magnitudes but also by swashplate inertia. Variation of 25% can occur in the magnitude of predicted 4/rev servo loads depending on the swashplate dynamics. Swashplate dynamics are particularly important for the prediction of higher frequencies of servo loads: 8 and 12/rev servo loads. Overprediction of 100–200% can occur in the magnitude of prediction depending on the swashplate dynamics. The 4/rev servo load, however, is affected primarily by the pitch-link loads. For the UH-60A rotor, it appears that the 5/rev component of pitch-link load dominates the 4/rev servo harmonic. This conclusion is consistent across the two flight conditions investigated in the present study.

References

[1] Kufeld, R. M., Balough, D. L., Cross, J. L., Studebaker, K. F., Jennison, C. D., and Bousman, W. G., Flight Testing the UH-60A Airloads Aircraft, *50th Annual Forum*, Vol. 1, American Helicopter Society, Alexandria, VA, May 1994, pp. 557–577.

[2] Kufeld, R. M., and Bousman, W. G., "UH-60A Airloads Program Azimuth Reference Correction," *Journal of the American Helicopter Society*, Vol. 50, No. 2, April 2005, pp. 211–213.

[3] Datta, A., and Chopra, I., "Validation of Structural and Aerodynamic Modeling Using UH-60A Airloads Program Data," *Journal of the American Helicopter Society*, Vol. 51, No. 1, Jan. 2006, pp. 43–58.

[4] Datta, A., and Chopra, I., "Prediction of UH-60A Main Rotor Structural Loads Using CFD/Comprehensive Analysis Coupling," *Journal of the American Helicopter Society*, Vol. 53, No. 4, Oct. 2008, pp. 351–365. doi:10.4050/JAHS.53.351

[5] Ormiston, R. A., "An Investigation of the Mechanical Airloads Problem for Evaluating Rotor Blade Structural Dynamics Analysis," *4th Decennial Specialist's Conference on Aeromechanics*, American Helicopter Society, Alexandria, VA, Jan. 2004, pp. 783–811.

[6] Ho, J. C., Yeo, H., and Ormiston, R. A., "Investigation of Rotor Blade Structural Dynamics and Modeling Based on Measured Airloads," *63rd Annual Forum*, American Helicopter Society, Alexandria, VA, May 2007, pp. 1720–1742.

[7] Sweers, J. E., "In-Flight Measurements and Correlation with Theory of Blade Airloads and Responses on the XH-51A Compound Helicopter Rotor. Vol. 3. Theoretical Prediction of Airloads and Structural Loads and Correlation with Flight Test Measurements," U.S. Army Aviation Material Lab. TR 68-22c, Lockheed-California Co., Burbank, CA, May 1968.

[8] Esculier, J., and Bousman, G., "Calculated and Measured Blade Structural Response on a Full-Scale Rotor," *Journal of the American Helicopter Society*, Vol. 33, No. 1, Jan. 1988, pp. 3–16.

[9] Torok, M. S., and Goodman, R. K., "Analysis of Rotor Blade Dynamics Using Model Scale UH-60A Airloads," *Journal of the American Helicopter Society*, Vol. 39, No. 1, Jan. 1994, pp. 63–69. doi:10.4050/JAHS.39.63

[10] Bauchau, O. A., and Kang, N. K., "A Multibody Formulation for Helicopter Structural Dynamic Analysis," *Journal of the American Helicopter Society*, Vol. 38, No. 2, April 1993, pp. 3–14. doi:10.4050/JAHS.38.3

[11] Hodges, D. H., "Geometrically Exact, Intrinsic Theory for Dynamics of Curved and Twisted Anisotropic Beams," *AIAA Journal*, Vol. 41, No. 6, June 2003, pp. 1131–1137. doi:10.2514/2.2054; also "Erratum: Geometrically Exact, Intrinsic Theory for Dynamics of Curved and Twisted Anisotropic Beams," *AIAA Journal*, Vol. 42, No. 7, July 2004, pp. 1500–1500. doi:10.2514/1.3032

[12] Johnson, W., "Rotorcraft Dynamics Models for a Comprehensive Analysis," *54th Annual Forum*, American Helicopter Society, Alexandria, VA, May 1998, pp. 452–471.

[13] Saberi, H., Khoshlahjeh, M., Ormiston, R. A., and Rutkowski, M. J., "Overview of RCAS and Application to Advanced Rotorcraft Problems," *4th Decennial Specialists' Conference on Aeromechanics*, American Helicopter Society, Alexandria, VA, Jan. 2004, pp. 741–781.

[14] Hodges, D. H., and Dowell, E. H., "Nonlinear Equations of Motion for the Elastic Bending and Torsion of Twisted Nonuniform Rotor Blades,"

NASA TN D-7818, Dec. 1974.

[15] Ormiston, R. A., Hodges, D. H., and Peters, D. A., "On the Nonlinear Deformation Geometry of Euler–Bernoulli Beams," NASA, TP 1566, 1980.

[16] Kvaternik, R. G., Kaza Krishna, R. V., "Nonlinear Curvature Expressions for Combined Flapwise Bending, Chordwise Bending, Torsion, and Extension of Twisted Rotor Blades," NASA TM X-73, 997, 1976.

[17] Kane, T. R., and Levinson, D. A., *Dynamics, Theory and Application*, McGraw–Hill, New York 1985.

[18] Cook, R. D., Malkus, D. S., and Plesha, M. E., "Concepts and Applications of Finite Element Analysis," *Finite Elements in Dynamics and Vibrations*, Wiley, New York, 1989, pp. 407–409.

[19] Bauchau, O. A., Bottasso, C., and Nikishkov, Y., "Modeling Rotorcraft Dynamics with Finite Element Multibody Procedures," *Mathematical and Computer Modelling*, Vol. 33, Nos. 10–11, May 2001, pp. 1113–1137.
doi:10.1016/S0895-7177(00)00303-4

[20] Ghiringhelli, G. L., Masarati, P., Mantegazza, P., and Nixon, M. W., "Multi-Body Analysis of Tiltrotor Configuration," *Nonlinear Dynamics*, Vol. 19, No. 4, Aug. 1999, pp. 333–357.
doi:10.1023/A:1008386219934

[21] Gere, J. M., and Timoshenko, S. P., "Mechanics of Materials," *Deflections of Beams*, 3rd ed., PWS Publishing, Boston, 1990, pp. 514–517.

[22] Dowell, E. H., Traybar, J., and Hodges, D. H., "An Experimental-Theoretical Correlation Study of Non-Linear Bending and Torsion Deformations of a Cantilever Beam," *Journal of Sound and Vibration*, Vol. 50, No. 4, Feb. 1977, pp. 533–544.
doi:10.1016/0022-460X(77)90501-6

[23] Dowell, E. H., and Traybar, J., "An Experimental Study of the Nonlinear Stiffness of a Rotor Blade Undergoing Flap, Lag, and Twist Deformations," NASA CR 137968, Jan. 1975, and NASA CR 137969, Dec. 1975.

[24] Hopkins, S. A., and Ormiston, R. A., "An Examination of Selected Problems in Rotor Blade Structural Mechanics and Dynamics," *Journal of the American Helicopter Society*, Vol. 51, No. 1, Jan. 2006, pp. 104–119.

[25] Kufeld, R. M., and Johnson, W., "The Effects of Control System Stiffness Models on the Dynamic Stall Behavior of a Helicopter," *Journal of the American Helicopter Society*, Vol. 45, No. 4, Oct. 2000, pp. 263–269.
doi:10.4050/JAHS.45.263

[26] Shanley, J. P., "Application of the Comprehensive Analytical Model of Rotorcraft Aerodynamics and Dynamics to the UH-60A Aircraft," Sikorsky Aircraft SER 72126, Feb. 1986.

[27] Stepniewski, W. Z., and Shinn, R. A., "A Comparative Study of Soviet vs Western Helicopters, Part 2: Evaluation of Weight, Maintainability and Design Aspects of Major Components," NASA CR 3580, March 1983.